



Lateral variations in crustal L_g attenuation in and around the Hangay Dome, Mongolia

Lei Zhang^{1,2} · Lian-Feng Zhao^{1,3} · Xiao-Bi Xie⁴ · Qing-Ju Wu⁵ · Zhen-Xing Yao¹

Received: 5 June 2021 / Accepted: 28 October 2021
© Geologische Vereinigung e.V. (GV) 2021

Abstract

The Hangay Dome in central Mongolia, a typical intraplate plateau far from plate boundaries, is characterized by rapid uplift and widespread volcanic activities in the Cenozoic. However, thermodynamics process for the landform in Cenozoic remains mysterious. Seismic L_g-wave, which is sensitive to crustal thermal status, can provide constraints on the crustal attenuation structure; thus, may be helpful to understand the thermodynamics. In this study, we estimate the L_g-wave quality factor Q_{L_g} across the Hangay Dome and its surroundings from 231 crustal earthquakes recorded by 136 regional broadband seismic stations distributed throughout north China and Mongolia. Using a joint tomographic method, we construct a broadband L_g attenuation model at 58 discrete frequencies distributed evenly in log scale between 0.1 and 20.0 Hz. The obtained Q_{L_g} model provides new insights into crustal attenuation in the region. The strong L_g wave attenuation observed in the northeastern Hangay Dome and western Gobi-Altai, associated with crust low-resistivity anomalies, low S-wave velocity region, heat flow and volcanic activities, suggest the existence of possible partial melting due to asthenospheric upwelling. The widespread moderately-low Q_{L_g} values around the perimeter of the Hangay Dome imply that the margin of the Hangay Dome has been weakened. The center part of the uplift is a small high Q_{L_g} nucleus, which is possibly the residue of the Precambrian basement. The above observations suggest that the Hangay Dome is lifted by small-scale asthenospheric upwellings. During this process, the very hot mantle materials strongly modified the Hangay Dome and also caused the Cenozoic volcanism and major earthquakes.

Keywords Hangay Dome in central Mongolia · Seismic L_g-wave · Seismic attenuation · Crustal thermal structures

✉ Lian-Feng Zhao
zhaolf@mail.iggcas.ac.cn

¹ Key Laboratory of Earth and Planetary Physics, Institute of Geology and Geophysics, Chinese Academy of Sciences, Beijing, China

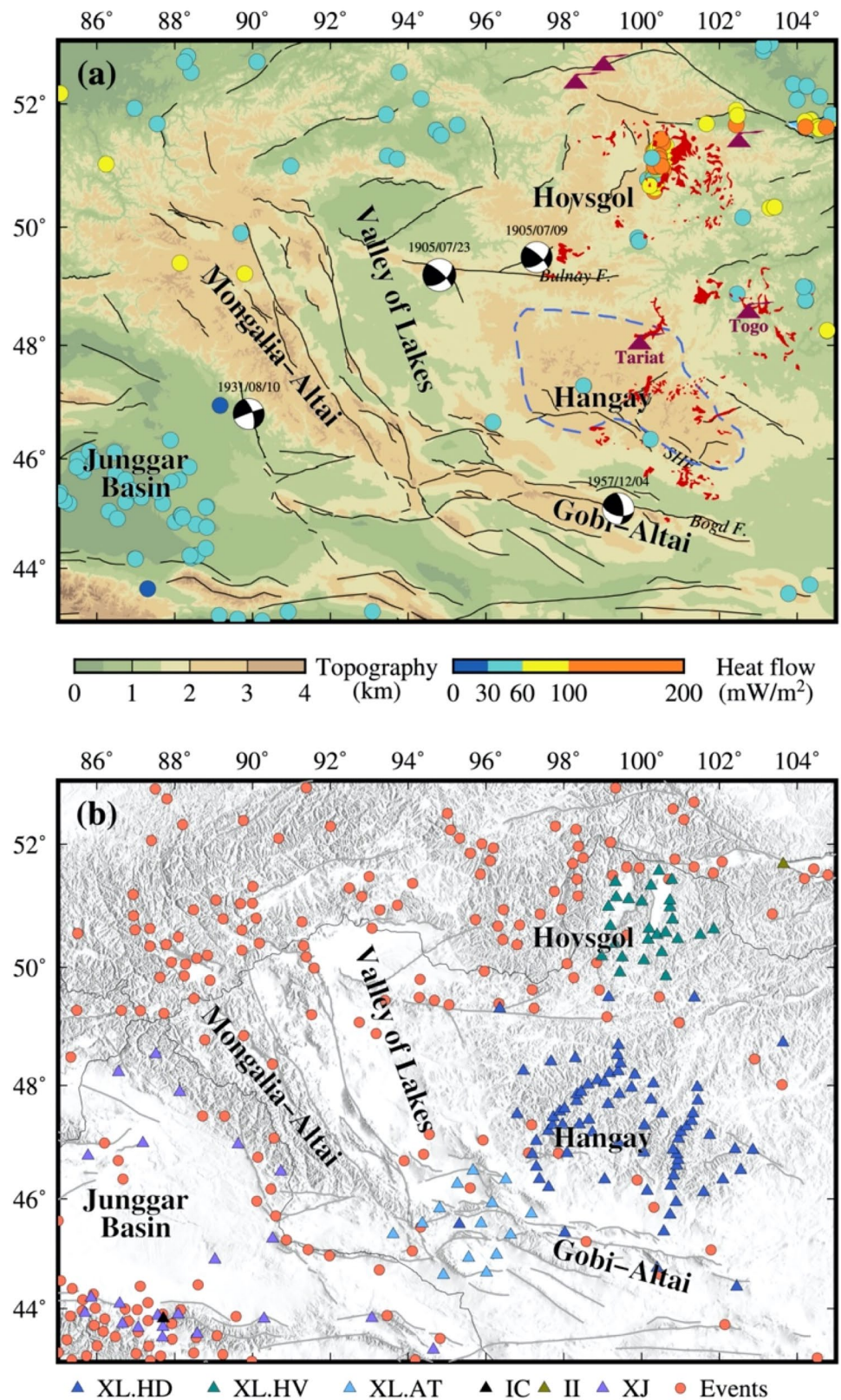
² College of Earth Sciences, University of Chinese Academy of Sciences, Beijing, China

³ Heilongjiang Mohe Observatory of Geophysics, Institute of Geology and Geophysics, Chinese Academy of Sciences, Beijing, China

⁴ Institute of Geophysics and Planetary Physics, University of California at Santa Cruz, Santa Cruz, CA, USA

⁵ Institute of Geophysics, China Earthquake Administration, Beijing, China

Fig. 1 **a** Map showing the Mongolian Plateau and its adjacent region overlain with major fault systems (black lines) and Holocene volcanoes (pink volcano symbols). The red colored patches are Cenozoic volcanic provinces (Ancuta et al. 2018). Four twentieth century earthquakes with magnitudes greater than 7.5 are shown by their moment tensor solutions (Guang-Yin et al. 2014; Rizza et al. 2015). The colored circles show the terrestrial heat flow values from the International Heat Flow Commission (IHFC) (Fuch et al. 2021). **b** Map showing the locations of the seismic stations (triangle) and events (orange circles) used in this study. The stations are color coded for different networks with their names are listed below the plot. The network XL.HD was deployed from June 10, 2012 to April 10, 2014. The networks XL.HV and XL.AT were deployed from August 5, 2014 to June 11, 2016



Introduction

The Hangay Dome, located in central Mongolia, is the broadest (~ 200,000 km²) upland on the Mongolian Plateau (Windley and Allen 1993). It is characterized by a high-elevation (average ~ 2500 m) and low-relief surface deep in the Asian continent between the Siberian Craton in the north, the India–Eurasia collisional zone 2000–3000 km away in the south, and the subduction zone of the Pacific plate ~ 2000 km away in the east (Fig. 1a). It is difficult to explain the uplift of the Hangay Dome in Cenozoic by the theory of plate tectonics. Furthermore, the elevated low-relief landscape also hosts a record of intermittent basaltic magmatism sourced from the sublithospheric mantle since 30 Ma (Barry et al. 2003; Ancuta et al. 2018). Various hypotheses have been proposed for the cause of Cenozoic deformation and volcanism in the Hangay Dome, including (1) the far-field stress associated with the India–Eurasia collision (Molnar and Tapponnier 1975), (2) the activities of isolated mantle plumes (Windley and Allen 1993), and (3) asthenospheric upwelling and lithospheric removal (Barry et al. 2003; Comeau et al. 2021; Feng 2021), but there is no consensus due to limited observations.

The Hangay Dome has a complex geological history, as it is located in the heart of the Central Asian Orogenic Belt, the largest accretionary orogen, which underwent massive continental growth in the Paleozoic (Xiao et al. 2018). The crust comprises Archean to early Proterozoic crystalline rocks modified by Paleozoic accretionary events involving the opening and closing of ocean basins in the Neoproterozoic and early Phanerozoic (1000–250 Ma) (Sengor et al. 1993; Windley et al. 2007). In the Cenozoic, it underwent active deformational processes and volcanism (Molnar and Tapponnier 1975; Barry et al. 2003; Calais et al. 2003; Ancuta et al. 2018). The GPS measurements reveal that the Hangay Dome, a kinematic transition zone between compressional deformation to the south and extension in the Baikal rift, moves eastward at ~ 4 mm/year (Calais et al. 2003). Such transition is accommodated by large strike-slip faults that bound the Hangay Dome. To the north is the left-lateral Bulnay fault, and to the south are the South Hangay fault and left-lateral Bogd fault systems (Bayasgalan et al. 1999). Three intracontinental earthquakes with magnitudes greater than 8.0 (1905/7/9 M_w 8.3 Bulnay, 1905/7/23 M_w 8.0 Tsetserleg, and 1957/12/04 M_w 8.1 Bogd) occurred along these faults in the early-middle twentieth century (Rizza et al. 2011 2015).

High-resolution and reliable images of crustal structure can provide useful insights into the mechanisms of surface uplift, active seismicity and volcanism in the Hangay Dome and its surroundings. The recent high-resolution magnetotelluric imaging of the crustal and upper mantle structure

showed wide spreading low-resistivity anomalies within the crust around the Hangay Dome and suggested localized asthenosphere upwellings in the crust (Käüfl et al. 2020). However, the knowledge on conductivity structure of the crust alone is not enough to picture the actual crustal properties. To obtain further constraints on crustal thermal structure and improve the understanding on Cenozoic deformation and volcanism of the Hangay Dome, high-resolution images of seismic attenuation property, which is sensitive to temperature, partial melting, fluid content and magma movement (Mitchell 1995), is highly demanded.

The Lg-wave is typically the most prominent seismic phase in high-frequency seismograms observed over continental paths at regional distances. It is usually understood as the sum of supercritical reflected S-waves trapped in the crustal waveguide (Xie and Lay 1994) or the surface wave overtones traveling in the continental crust (Knopoff et al. 1973). As it samples the whole crust and is insensitive to source radiation patterns when the magnitude is moderate (Furumura and Kennett 1997), Lg-waves provide an ideal tool to study the amplitude variations during seismic waves propagating within the continental crust, and have been widely used to investigate crustal seismic attenuation (Xie et al. 2004; Zhao et al. 2010 2013a; Gallegos et al. 2014; Kaviani et al. 2015; He et al. 2021). Lg-wave attenuation is generally quantified by the frequency-dependent quality factor Q_{Lg} . Low Q_{Lg} values denote strong attenuation, which is generally associated with thick sediments (Mitchell and Hwang 1987), complex fault systems (Mitchell 1995; Bao et al. 2012), or partial melts characterized by high temperatures and low viscosities (Xie et al. 2004; Zhao et al. 2013a), while high Q_{Lg} values denote weak attenuation and correlate well with a stable block (e.g., Zhao et al. 2013b).

Rapine and Ni (2003) testified that Lg-waves propagate efficiently at regional distances for Mongolian region, validating the investigations into Lg attenuation in the Hangay Dome. Unfortunately, a high-resolution Lg-wave attenuation model is lacking due to the limitation of sparse stations. To date, our knowledge on the Lg-wave attenuation structure on the Mongolian Plateau is mainly from Lg-wave attenuation studies in Eurasia, whose resolution is not high enough to image the regional lateral variations on the Mongolian Plateau. Mitchell et al. (1997, 2008) obtained a 1 Hz coda Q map in Eurasia and showed stable Q_0 values (Q values at 1 Hz) between approximately 400 and 600 in the Mongolian region. Xie et al. (2006) measured Q_0 values of Lg-waves with the two-station method using the power-law attenuation model $Q(f) = Q_0 f^n$, and the results in the Mongolian region were also between approximately 400 and 600. Sparse stations limited the resolution of these two models, and lateral variations in the Mongolian region were not observed. Taylor et al. (2003) further investigated the 1 Hz Q_{Lg} model in East Asia with Bayesian Lg attenuation tomography based on the

background model (Mitchell et al. 1997) and found slight lateral variations on the Mongolian Plateau (~550) and in the nearby Baikal rift (~450). Phillips et al. (2005) provided a Q_{Lg} model in central and eastern Asia using the amplitude ratio technique, and the resolution, on average, was 2.5° . This model at 1 Hz, however, shows dramatic lateral variations in the Mongolian region, with low Q (~300) at the Baikal rift and high Q (~800) at Mongol–Okhotsk. Clearly, there are great differences between these models, which provide a Q_{Lg} model only around 1 Hz. He et al. (2017) presented the frequency-dependent Q_{Lg} and Q_{Sn} models and found low crustal attenuation in the Hentey Mountains, but the region of the model was limited to the eastern Mongolian Plateau.

The Central Mongolia Seismic Experiment, originally designed to determine the structure and composition of the lithosphere and sublithospheric mantle beneath the central and western Mongolia, deployed 3 subarrays consisting of total 112 broadband seismic stations from 2012 to 2016 (network code: XL). Benefitted from this project, we were provided with an unprecedented opportunity to image the crustal Lg-wave attenuation structure beneath the Hangay Dome and its surroundings at a much higher resolution. In this study, we used the data from regional seismic stations including XL stations to develop a high-resolution broadband Lg-wave attenuation model between 0.1 and 20.0 Hz for the Hangay Dome and its surroundings. This model is expected to give further constraint on thermal activities beneath the Hangay Dome and its surroundings, shedding light on the regional geodynamics of the uplift and volcanism of the Hangay Dome.

Data and method

Regional datasets

To investigate the frequency-dependent Q_{Lg} for the Hangay Dome and its surroundings, we collected more than 14,000 vertical-component broadband seismograms generated by 231 crustal earthquakes in northeast China and Mongolia occurred between June 2012 and March 2016, recorded by the XL network during its deployment, the XJ network from the China Earthquake Network Center (CENC) and two permanent stations IC.WMQ and II.TLY from the Incorporated Research Institutions for Seismology (IRIS) data management center. All these stations were equipped with broadband digital seismographs. The magnitudes of these earthquakes were ranged from 3.6 to 6.0, and their focal depths were shallower than the Moho discontinuity given by CRUST1.0 (Laske et al. 2013) to ensure they were crustal events. The waveform data were selected with their epicentral distances between 300 and 2000 km. Within this range, the Lg-waves were usually the most prominent phase

in regional seismograms. The dense event distribution and available stations generated dense ray coverage over the majority of the study region, providing an ideal condition for a high-resolution Lg-wave attenuation tomography.

Lg-wave spectrum

To process the waveform data, we first remove the trends, means, and instrument responses from raw vertical-component seismograms (Goldstein and Snoke 2005). To locate the Lg signal in the waveform, we use a 0.6 km/s-long group velocity window to scan the waveform between group velocities 3.7 and 2.9 km/s and calculate the waveform energy within the window. The section of waveform which gives the maximum energy will be used as the Lg-wave signal. Next, both pre-Pn and pre-Lg noises were picked using windows with the same length as the Lg window for noise analysis. The pre-Pn noise window ends at group velocity 8.4 km/s and the pre-Lg noise ends at the start of Lg window. The Fast Fourier Transform (FFT) was performed on the Lg-signal, as well as the pre-P and pre-Lg noise series. Spectral amplitudes of the Lg signal and noises were extracted from these spectra at 58 discrete frequencies log-evenly distributed between 0.1 and 20.0 Hz. Two signal-to-noise ratios (SNR) were used to quality control the data. The Lg waves with their SNR to pre-P noise less than 2 or SNR to pre-Lg noise less than 1.0 were removed to exclude Lg-signals seriously affected by the background noise or coda waves of previous phases (Luo et al. 2021). The Pre-P noise was also used to perform noise corrections to the Lg-wave. By assuming that: (1) the seismic signal is superimposed by the noise, (2) the noise is stationary over a certain time period, and (3) the noise is random and uncorrelated with the signal, the correction can be performed using $A_S^2(f) = A_O^2(f) - A_N^2(f)$, where $A(f)$ is the spectral amplitudes at frequency f and its subscripts S , O , and N denote the true signal, the observed data, and the pre-P noise, respectively (Ringdal et al. 1992; Schlittenhardt 2001; Zhao et al. 2008). As an example, Fig. 2 illustrates this process, where Fig. 2a is a 0.5–5.0 Hz filtered velocity waveform recorded at an epicentral distance of 356 km and Fig. 2b is the related envelope. Figure 2c–e are windowed Lg-signal and the pre-P and pre-Lg noise series. Figure 2f shows amplitude spectra of the Lg-signal and noises, in which the gray lines are raw spectra calculated from the FFT and the symbols are extracted discrete spectra at 58 frequencies. After rejected Lg records below the SNR threshold criteria, we further required that an event be recorded at least by three stations and a station recorded at least three events. After these, the dataset for attenuation tomography consists of 13,686 high-quality waveforms from 231 crustal earthquakes recorded at 136 broadband seismic stations throughout Northeast China and Mongolia. Figure 1b illustrates the locations of events and stations used in this study, with all event parameters listed in Table S1.

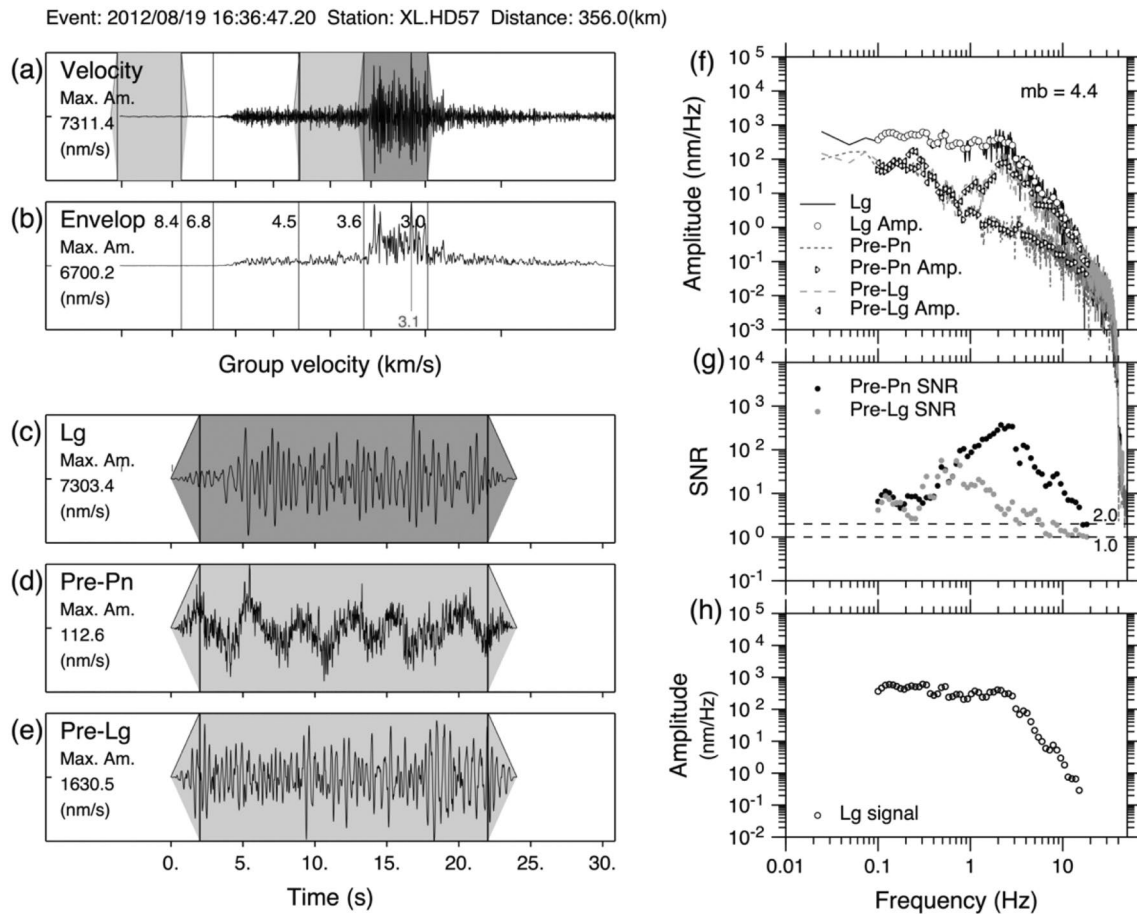


Fig. 2 A sample data preprocessing procedure. **a** Velocity record after deconvolving with the instrument response. **b** Envelope of the waveform filtered between 0.5–5.0 Hz. It will be used to find the maximum energy arrival in the Lg sampling window. **c–e** Windowed Lg signal, and pre-Pn and pre-Lg noise, **f** Lg-wave and noise spectra,

where gray lines are raw spectra and symbols are extracted discrete spectral values. **g** Signal-to-noise ratios, and **h** noise-corrected Lg-wave spectrum. Note that the data points with their pre-Pn SNR lower than 2.0 or their pre-Lg SNR lower than 1.0 are dropped

Single-station data

The Lg-wave spectral amplitude at frequency f recorded by station i from event k can be expressed as

$$A_{ki}(f, \Delta) = S_k(f)G_{ki}(\Delta)\Gamma_{ki}(f, \Delta)P_i(f)r_{ki}(f), \quad (1)$$

where Δ is the epicentral distance, $S_k(f)$ is the source term, $G_{ki}(\Delta)$ is the geometrical spreading factor, $\Gamma_{ki}(f, \Delta)$ is the attenuation term, $P_i(f)$ is the site response and $r_{ki}(f)$ is the random errors in the data which may come from variety of sources such as the ambient noise, source properties biased from the standard model, station locations away from a great circle path, etc. The radiation pattern of the source is not included in the formulation because the Lg-wave is composed of very wide incident angles, thus is not strongly affected by the radiation pattern (Castro et al. 1990).

Considering its highly reverberated propagation mechanism, the geometrical spreading for Lg-wave is difficult to obtain, instead, the below simplified formulation is used (Street et al. 1975; Herrmann and Kijko 1983)

$$G_{ki}(\Delta) = (\Delta_0\Delta_{ki})^{-\frac{1}{2}}, \quad (2)$$

where Δ_0 represents a reference distance fixed at 100 km.

The attenuation factor $\Gamma_{ki}(f, \Delta)$ can be expressed by (Zhao et al. 2013b).

$$\Gamma_{ki}(f, \Delta) = \exp\left(\frac{-\pi f}{v} \int_k^i \frac{ds}{Q(x, y, f)}\right) \quad (3)$$

where v is the Lg-wave group velocity, $\int_k^i ds$ is the integral along the great circle path from event k to station i , $Q(x, y, f)$ is the Lg-wave apparent quality factor and x and y are geographic coordinates.

Two-station data

To address the tradeoff between the source and attenuation terms, the two-station dataset is also calculated, which can improve the reliability of the estimated Q by removing the source term. When both stations i and j record the same event k , and the locations of stations and event are approximately aligned on a great circle, the interstation amplitude ratio from station i to j can be calculated by (Zhao et al. 2013b)

$$A_{ij} = \frac{A_{kj}}{A_{ki}} \approx \left(\frac{\Delta_{kj}}{\Delta_{ki}} \right)^{-\frac{1}{2}} \cdot \exp\left(\frac{-\pi f}{v} \int_i^j \frac{ds}{Q(x, y, f)} \right) \cdot \frac{P_j}{P_i} \cdot \frac{r_{kj}}{r_{ki}} \quad (4)$$

where A_{kj} and A_{ki} are observed amplitudes at stations j and i from a common event k , respectively; Δ_{kj} and Δ_{ki} are epicentral distances from event k to stations j and i , $\int_i^j ds$ is the integral along the great circle path from station i to j , P_j and P_i are the site responses at stations j and i , and r_{kj} and r_{ki} are random errors along the paths from event k to stations j and i , respectively.

Lg wave Q tomography

Based on the perturbation theory, we establish an inversion system for Lg-wave Q tomography. By neglecting the random effects along the Lg propagation path, i.e., letting $r_{ki}(f) = 1$, applying the natural logarithm to Eq. (1) and combining with Eq. (3), we obtain a linearized system

$$\ln[A_{ki}(f, \Delta)] = \ln[S_k(f)] + \ln[G_{ki}(\Delta)] - \frac{\pi f}{v} \int_k^i \frac{ds}{Q(x, y, f)} + \ln[P_i(f)] \quad (5)$$

Assuming that the attenuation, source function and site response can be separated into a background part (denoted by superscript 0) and a perturbation (Zhao et al. 2013b),

$$\frac{1}{Q(x, y, f)} \approx \frac{1}{Q^0(x, y, f)} - \frac{\delta Q(x, y, f)}{[Q^0(x, y, f)]^2} \quad (6)$$

$$\ln[S_k(f)] = \ln[S_k^0(f)] + \delta \ln[S_k(f)] \quad (7)$$

$$\ln[P_i(f)] = \ln[P_i^0(f)] + \delta \ln[P_i(f)] \quad (8)$$

Substituting Eqs. (6)–(8) into Eq. (5), we have

$$\ln[A_{ki}(f, \Delta)] = \ln[A_{ki}^0(f, \Delta)] + \delta \ln[S_k(f)] - \frac{\pi f}{v} \int_k^i \frac{\delta Q(x, y, f)}{[Q^0(x, y, f)]^2} ds + \delta \ln[P_i(f)] \quad (9)$$

where

$$\ln[A_{ki}^0(f, \Delta)] = \ln[S_k^0(f)] + \ln[G_{ki}(\Delta)] - \frac{\pi f}{v} \int_k^i \frac{ds}{Q^0(x, y, f)} + \ln[P_i^0(f)] \quad (10)$$

Then, the difference in spectral amplitude before and after the Q , $\ln S$ and $\ln P$ are perturbed is

$$\begin{aligned} \delta \ln[A_{ki}(f, \Delta)] &= \ln[A_{ki}(f, \Delta)] - \ln[A_{ki}^0(f, \Delta)] \\ &= \delta \ln[S_k(f)] - \frac{\pi f}{v} \int_k^i \frac{\delta Q(x, y, f)}{[Q^0(x, y, f)]^2} ds \\ &\quad + \delta \ln[P_i(f)] \end{aligned} \quad (11)$$

Therefore, we can relate the perturbations in the attenuation, source, and site response with the amplitude residual. We denote the amplitude residual $\delta \ln[A_{ki}(f, \Delta)]$ as $\bar{h}_{ki}(f)$ for event k recorded by station i at frequency f . It can be distributed to the path based on the mesh discretization:

$$\bar{h}_{ki}(f) = \sum_{n=1}^N [a_{in} \cdot \delta Q_n] + e_k \cdot \delta \ln[S_k(f)] + u_i \cdot \delta \ln[P_i(f)] \quad (12)$$

where n is the index of a grid point, N is the total number of grids a ray passes, $a_{in} = -\frac{\pi f}{v} \frac{D_n}{(Q^0(x_n, y_n, f))^2}$, x_n and y_n are the coordinates of grid n , and D_n denote the length of a ray section in grid n , e_k , and u_i are coefficients for the source k and station i , respectively, with $u_i = e_k = 1$ for single-station data. Finally, the linear equations for a single-station dataset can be expressed as.

$$\mathbf{H}_s = \mathbf{A}_s \cdot \delta \mathbf{Q} + \mathbf{E}_s \cdot \delta \mathbf{S} + \mathbf{U}_s \cdot \delta \mathbf{P} \quad (13)$$

where \mathbf{H}_s is a vector composed of residuals of logarithmic spectra data, $\delta \mathbf{Q}$ is a vector composed of the perturbations of the Q models, matrix \mathbf{A}_s is composed of elements a_{in} , sets up the relationship between Q perturbations and the observed single-station Lg-wave spectra, matrix \mathbf{E}_s sets up the relationship between source perturbation and the observed single-station Lg-wave spectra, $\delta \mathbf{S}$ is a vector composed of the perturbations of the logarithmic source terms, matrix \mathbf{U}_s sets up the relationship between site responses and the observed single-station Lg-wave spectra, and $\delta \mathbf{P}$ is a vector composed of the perturbations of the logarithmic site responses.

For two-station measurements, the source term is eliminated by taking spectral ratios. A similar matrix equation can be obtained.

$$H_t = A_t \cdot \delta Q + U_t \cdot \delta P \tag{14}$$

where H_t is a vector composed of residuals of logarithmic spectral ratios, matrix A_t sets up the relationship between interstation Q perturbations and the residuals of the logarithmic Lg-wave spectra ratios, matrix U_t sets up the relationship between site responses and the observed Lg-wave spectra ratios, and δP is a vector composed of the difference between the perturbations of logarithmic site responses of two stations.

The sum of all logarithmic site responses $\sum_{i=1}^N \ln P_i$ can be assumed zero, when the stations are evenly distributed in the study area (Ottmöller 2002; Ottmöller et al. 2002; Zhao and Xie 2016; Zhao and Mousavi 2018). Therefore, based on the assumption that the sum of the perturbation of site responses (in logarithm) $\sum_{i=1}^N \delta \ln P_i = 0$, and simultaneously controlling a relative variation of the site responses, $\sum_{i=1}^N \delta |\ln P_i| < \epsilon$, where ϵ is an empirical value for normalizing the site responses, the site response terms δP for both single- and two-station data are ignored in the inversion.

Therefore, by combining eqs. 13 and 14, we have.

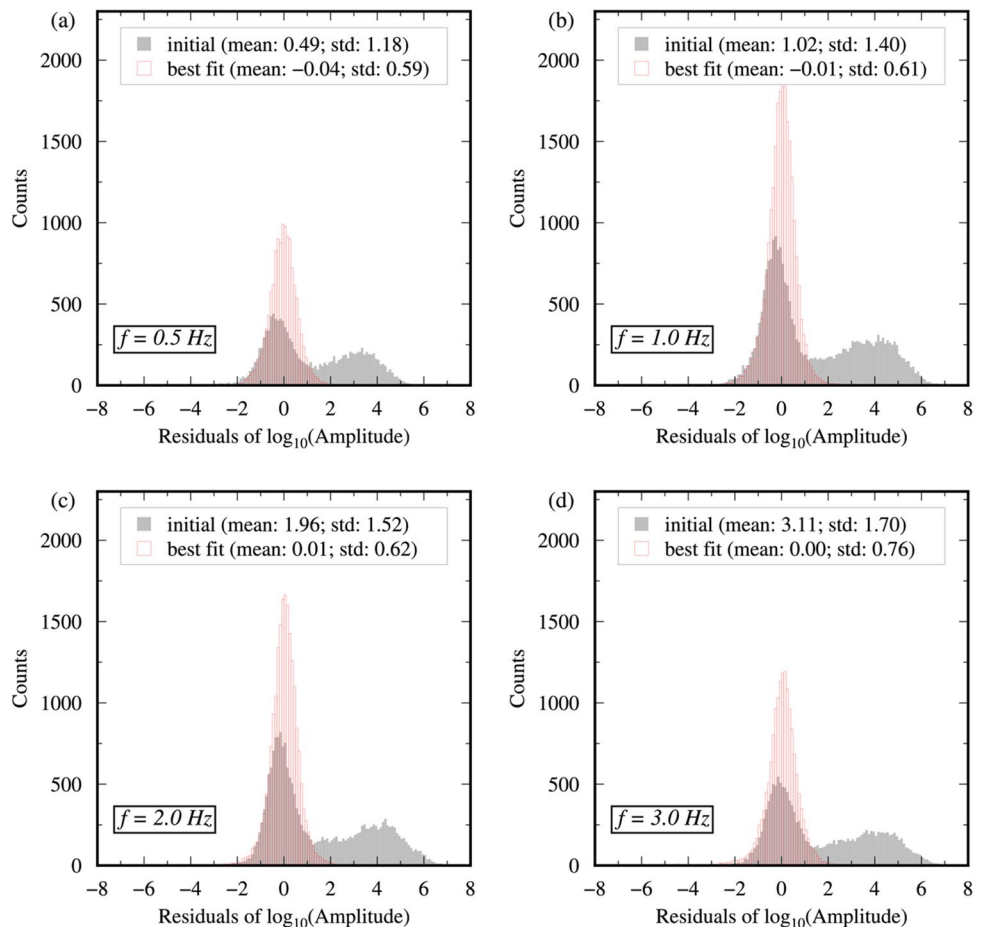
$$\begin{bmatrix} H_s \\ H_t \end{bmatrix} = \begin{bmatrix} A_s \\ A_t \end{bmatrix} \cdot \delta Q + \begin{bmatrix} E_s \\ 0 \end{bmatrix} \cdot \delta S. \tag{15}$$

We used a tomography approach which jointly inverts the regional Q and source excitation terms using both single- and two-station data to reduce the attenuation-source tradeoffs (Zhao et al. 2013a). A regional average Q obtained from the two-station dataset is used as the initial model. The Least Squares QR factorization (LSQR) algorithm, including the regularization, damping and smoothing, is used to solve the linear system (Paige and Saunders 1982) and update both attenuation and source terms in an iterative manner. At each frequency, we calculate a total of 250 iterations, and the result is chosen based on the smallest residual error. To evaluate the resulted source spectra, we further fit the solved source spectrum for each event with an ω^{-2} source model (Brune 1970)

$$S(f) = \frac{M_0}{4\pi\rho v_s^3} \cdot \frac{1}{\left(1 + \frac{f}{f_c}\right)^2}, \tag{16}$$

where M_0 is the scalar seismic moment and f_c is the corner frequency. The density and S-wave velocity are assumed

Fig. 3 Histograms of the Lg spectral amplitude misfits before (solid gray) and after (open red) inversions, with **a** 0.5, **b** 1.0, **c** 2.0, and **d** 3.0 Hz, respectively



to be $\rho = 2.7\text{g/cm}^3$ and $v_s = 3.5\text{km/s}$. The resulted source parameters for all events are listed in Table S1. After the inversion, the data residuals are largely reduced and their distribution tends to be a Gaussian function with a zero mean and a much smaller standard deviation (Fig. 3). This implies a better data fit after inversion. The remaining unsolved residuals may be resulted from complex source processes, site responses, and other random effects, which are neglected in our joint inversion (e.g., Zhao and Mousavi 2018).

Resolution analysis

Using a checkerboard method, we conduct resolution analysis to test the constrain of the current regional dataset to the inverted Q_{Lg} model. We first create a checkerboard-shaped Lg-wave attenuation model by adding 7% logarithmic positive/negative perturbations to a constant background Q_{Lg} model (Zelt 1998; Morgan et al. 2002; Zhou et al. 2011; Zhao et al. 2013a; Liu et al. 2014). Then, Eq. (1) is used to calculate synthetic Lg spectral amplitudes, where ray paths are from the actual observation geometry, and source terms including their scalar seismic moments and corner frequencies are adopted from the inverted source spectra. Random noise with 7% rms perturbation is added to the synthetic Lg-wave spectra. The two-station data are extracted from the synthetic single-station data. Inverting the two- and single-station synthetic data simultaneously, we obtain the Q_{Lg} model, which is compared with the original checkerboard model to provide a resolution analysis. Our broadband

Lg-wave attenuation tomography is calculated independently at 58 discrete frequencies. Because the source spectrum, the noise level and the attenuation are all frequency dependent, the number of available rays vary dramatically across the entire frequency band. The resolution at each frequency is different. Figure 4 summarizes the number of available ray paths versus frequencies between 0.1 and 20.0 Hz, including single-station, two-station and combined datasets. We conduct resolution tests for all 58 individual frequencies using a series of checkerboard models with different grid sizes varying from $0.5^\circ \times 0.5^\circ$ to $0.2^\circ \times 0.2^\circ$ at an increment of 0.5° . The shaded area in Fig. 4 highlights the 0.4–6.0 Hz band, within which the data have the maximum ray density and give the highest resolution.

Results

Based on the aforementioned data set and the Lg-wave tomography method, we obtain a broadband attenuation model for the Hangay Dome and its surrounding regions at 58 discrete frequencies between 0.1 and 20.0 Hz.

Q_{Lg} distributions at individual frequencies

Figure 5 illustrates the Q_{Lg} maps, checkerboard resolution tests and ray-path coverages at 0.5, 1.0, 2.0, and 3.0 Hz, respectively. Note that different color scale is used for each frequency. The blue rays are for the single-station data and the red rays are for two-station data. The spatial resolution also varies with frequency as the ray-path coverage varies. Generally, Q_{Lg} distributions at different frequencies show similar patterns for large-scale lateral variations, which correlate well with the regional tectonics. The Junggar Basin, consisting of trapped oceanic crust formed in the Paleozoic (Xiao et al. 2018), is characterized by relatively high Q_{Lg} values at all frequencies. A high Q_{Lg} anomaly can be observed beneath the Hangay Dome and Gobi–Altai at 0.5 and 1.0 Hz. With the increase in the frequency, this high Q_{Lg} anomaly is separated into two parts beneath the Hangay Dome and Gobi–Altai, respectively. The high- Q_{Lg} anomaly in the Gobi–Altai at 2.0 and 3.0 Hz corresponds to a high-resistivity area in the crust (Käufel et al. 2020). Both two blocks are considered stable due to their relatively low heat flow values between ~ 40 and 50mW/m^2 (from International Heat Flow Commission, IHFC). In contrast, low Q_{Lg} values are observed underneath the Hovsgol rift and Bulnay fault system. The low- Q_{Lg} anomaly linked to the Hovsgol rift, especially its eastern part, corresponds to the high heat flow of approximately 120mW/m^2 and abundant basalt outcrops. The Valley of Lakes and the Mongolia–Altai also feature

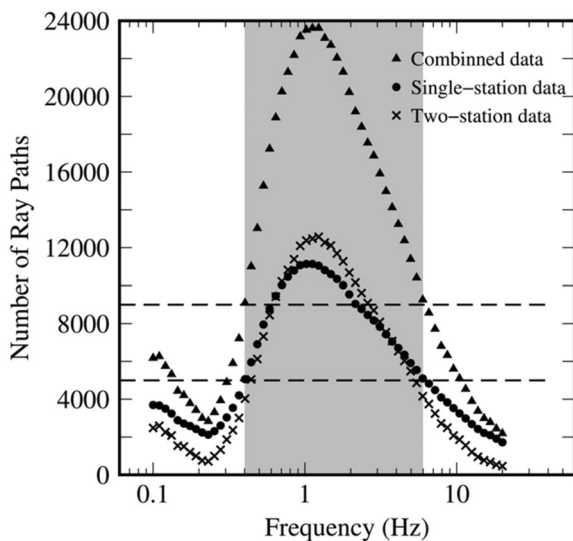


Fig. 4 The numbers of available rays, including both single-station and two-station rays, at individual frequencies from 0.1 to 20.0 Hz. The shaded area highlights the 0.4–6.0 Hz band, within which the resolution can reach to $\sim 1.0^\circ \times 1.0^\circ$

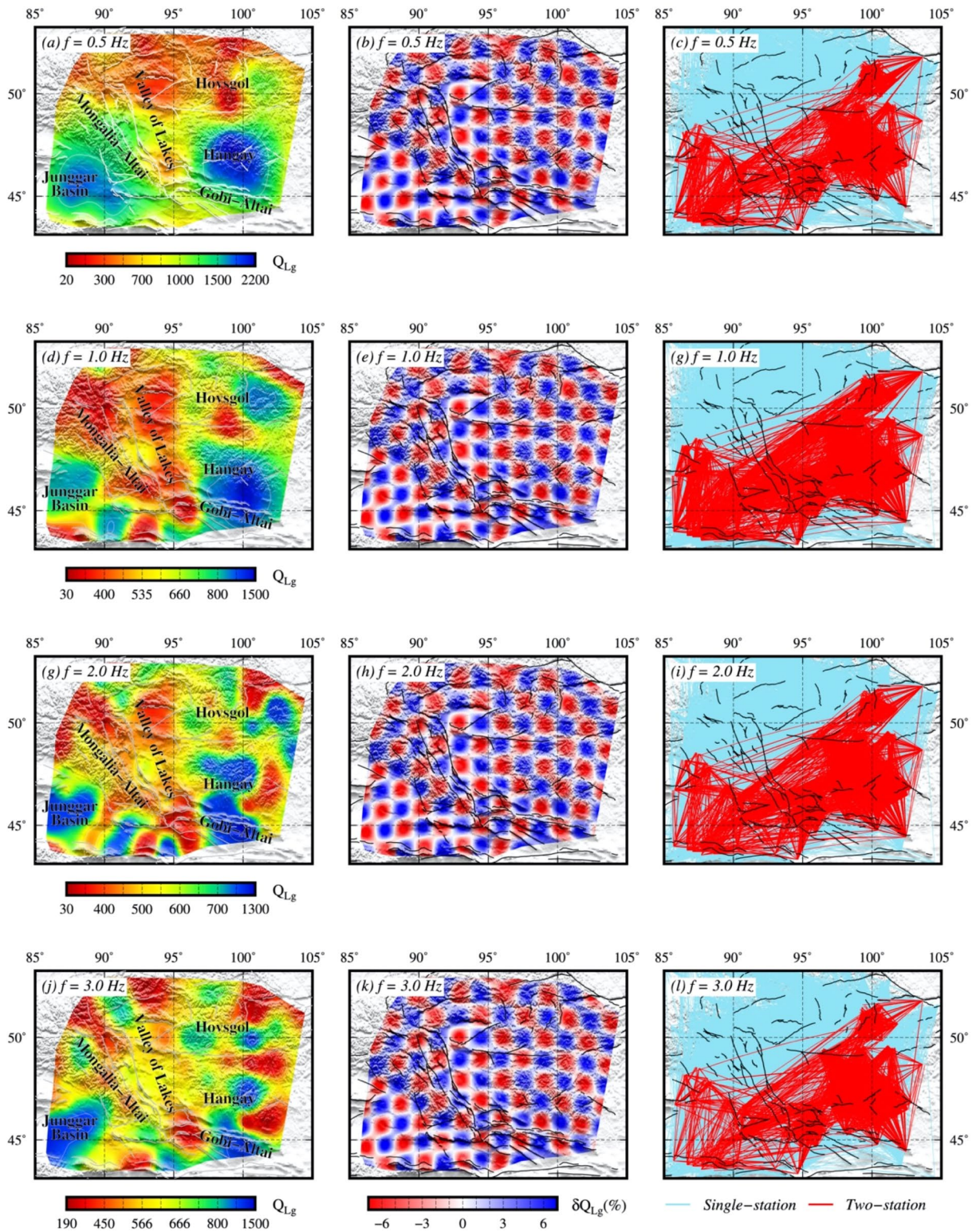


Fig. 5 Lateral variations of Q_{Lg} (left panel), checkerboard resolution analysis (center panel), and ray-path coverage (right panel) at 0.5 Hz (a–c), 1.0 Hz (d–f), 2.0 Hz (g–i), and 3.0 Hz (j–l). Note that the Q_{Lg}

maps at different frequencies use different color scales. The checkerboard analysis resolution is $1.0^\circ \times 1.0^\circ$. The blue and red rays are for single-station and two-station data

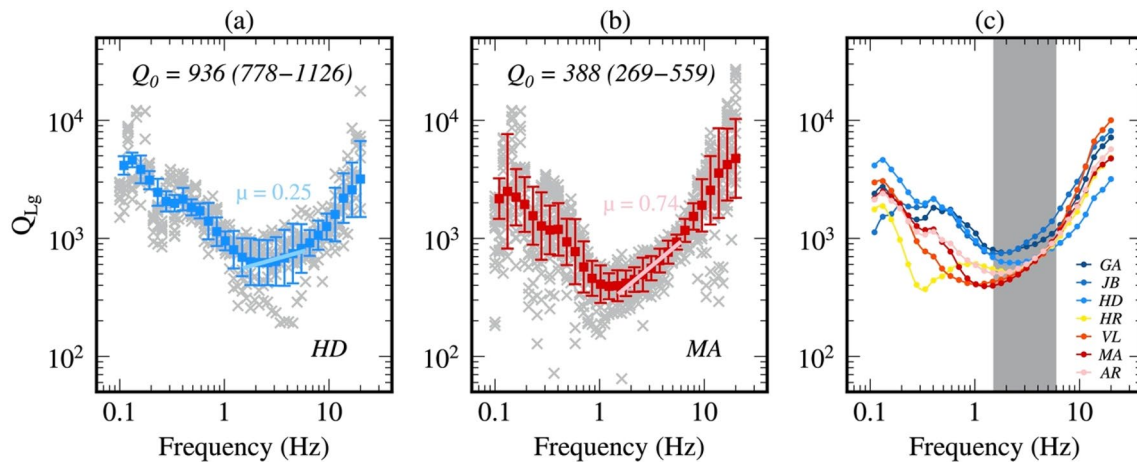


Fig. 6 Frequency-dependent Q_{Lg} for selected blocks, with **a** Hangay Dome and **b** Mongolia–Altai. **c** Comparison of average Q_{Lg} values in all blocks. The shaded area highlights the 1.5–6.0 Hz frequency band,

within which the data provide high ray-coverage density and the resolution can reach to $1.0^\circ \times 1.0^\circ$. For detailed properties in individual blocks refer to Table 1

Table 1 Lg-wave Q for individual geological blocks

	Lg-wave Q model			CRUST1.0 model ^a		IHFC ^b	
	Q_0	Q	η	crustal	sediment	heat flow	
Block name	Abbr	(1 Hz Q)	(1.5–6 Hz)	(1.5–6 Hz)	thickness (km)	thickness (km)	(mW/m ²)
Gobi–Altai	GA	1028 (810–1305)	999 (612–1632)	0.36 ± 0.23	46.7 ± 0.5	0.1 ± 0.1	–
Junggar Basin	JB	796 (654–969)	966 (645–1447)	0.59 ± 0.21	43.5 ± 5.7	2.6 ± 2.7	46.3 ± 6.2
Hangay Dome	HD	936 (778–1126)	833 (487–1424)	0.25 ± 0.14	51.3 ± 0.9	0.0 ± 0.0	45.3 ± 6.4
Hovsgol rift	HR	648 (488–861)	590 (366–952)	0.49 ± 0.21	49.2 ± 1.8	0.0 ± 0.0	96.7 ± 68.2
Valley of Lakes	VL	425 (364–495)	585 (418–819)	0.59 ± 0.18	47.1 ± 2.1	0.2 ± 0.3	40.0 ± 6.0
Mongolia–Altai	MA	388 (269–559)	504 (315–807)	0.74 ± 0.19	48.1 ± 2.5	0.0 ± 0.1	65.0 ± 23.5
All regions	AR	537 (292–986)	626 (376–1040)	0.55 ± 0.06	47.5 ± 3.2	0.4 ± 1.1	75.8 ± 57.7

^aFrom Laske et al. (2013)

^bFrom the Global Heat Flow Database maintained by International Heat Flow Commission, IHFC (<https://ihfc-iugg.org/products/global-heat-flow-database>)

relatively low Q_{Lg} values, corresponding to relatively high surface heat flows between 60 and 70 mW/m². Farther south, the Gobi–Altai conductor (GAC), a junction between the Gobi–Altai and Mongolia–Altai, shows complex fault systems and high seismic activities. Its low Q_{Lg} values is consistent with low-resistivity anomalies recently detected by magnetotelluric method in this region (Käufel et al. 2020).

Frequency dependence of the Lg-wave attenuation

The tomography results at 58 individual frequencies from 0.1 to 20.0 Hz enable us to investigate the frequency dependency of the Lg-wave attenuation. The averaged Q_{Lg} values versus frequency in selected tectonic regions are given in Fig. 6. The light gray crosses in Fig. 6a, b are directly inverted Q_{Lg} values in two selected blocks (labeled in the lower right in each panel). The colored

squares and error bars are their mean values and standard deviations at different frequencies in the logarithmic scale. The Q_0 values and standard deviations are also labeled in Figs. 6a, b. Figure 6c compares the average Q_{Lg} versus the frequency for all geology units, with their results also listed in Table 1. By averaging values from all blocks in the entire study region, the regional averaged Q_{Lg} versus frequency can be obtained (the curve labeled with AR in Fig. 6c). The regional average Q_{Lg} is 537 with upper and lower standard deviations of 292 and 986, respectively. This value is much higher than those from active orogenic regions and marginal seas (Zhao et al. 2013a; Zhao and Xie 2016; He et al. 2021; Luo et al. 2021), indicating a generally stable intracontinental orogenic region. Within the study region, geology units with their average Q_{Lg} lower than the regional average, e.g., the Mongolia–Altai, Valley of Lakes and Hovsgol rift, tend to be more tectonically

active. In contrast, the relatively stable blocks, such as the Junggar Basin, Hangay Dome and Gobi–Altai, manifest average Q_0 values higher than the regional average. Notably, the Mongolia–Altai and Gobi–Altai show different attenuation characteristics, indicating different orogenic mechanisms between them. The variations in Lg-wave attenuations across different geology units reveal significant lateral variations in underlying processes.

In many earlier works, limited by the band width of the instruments and coverage of the seismic data, the attenuation model is often limited to a narrow frequency band around a central frequency and a power-law model $Q(f) = Q_0 f^\eta$ is often used (Castro et al. 1990; Xie et al. 2006). The model provided here has a very-wide frequency band. At frequencies less than 1.5 Hz, the Q_{Lg} values decrease as the frequency increases resulting in a negative η in this frequency band, consisting with some previous Lg-wave attenuation studies in Mongolia (Xie et al. 2006). He et al. (2017) also found negative η in several regions in east Mongolia, and suggested it may be related to volcanic activities. In addition, similar negative η was also observed between frequencies 0.1 and 0.3 Hz in several places in the southeastern Tibetan Plateau, corresponding to regions with thick crust (> 45 km) and thin sedimentary layers (< 0.1 km) (He et al. 2021). The negative η can also be observed in North Arabia Plate and India Shield (Zor et al. 2007; Pasyanos et al. 2009). One possible explanation is that scattering causes complex frequency-dependent attenuation which is linked to the correlation structures of scatters (Pasyanos et al. 2009). In this study, the observed negative η at frequencies lower than 1.5 Hz may be resulted from the microseism noise. Meltzer et al. (2019) investigated the data quality in network XL and found the noise power significantly increases in the microseism band between 0.1 and 1.5 Hz, highly correlating to the frequency band where negative η appears. Overall, the negative η has been observed in many studies, but its origin is remained unsolved and need further investigation. To quantify the analysis, we select the band from 1.5 to 6.0 Hz to analyze the frequency dependence, where the general trend that the Q_{Lg} increases with the increase of frequency is maintained, and the maximum resolution of $1.0^\circ \times 1.0^\circ$ is reached. The linear regression is calculated based on the power-law relation (Benz et al. 1997) on the double logarithmic scale

$$Q(f) = Q_r \left(\frac{f}{f_r} \right)^\eta \quad (17)$$

where Q_r is the Q at a reference frequency f_r , and η is assumed to be a constant over the interest frequency band. If taking $f_r = 1.5$ Hz, the resulting η ranges from 0.35 to 0.74 for different blocks (Table 1). A regional averaged power-law

Q model of $Q(f) = 420_{398}^{443} (f/1.5)^{0.55 \pm 0.06}$ is consistent with previous Lg-wave attenuation study in this region (Mitchell et al. 2008).

Broadband Q_{Lg} images

We plot the broadband Q_{Lg} in comparison with the surface topography, crust and lithosphere–asthenosphere boundary (LAB) and seismic P-wave velocity structures (Fig. 7). A broadband Q_{Lg} map obtained by averaging the Q_{Lg} values within the frequency range 1.5–6.0 Hz is shown in Fig. 7a, overlaid with major fault systems (white lines), four major twentieth century earthquakes, Holocene volcanoes (red volcano signs), Cenozoic basalts (light pink patches, Ancuta et al. 2018). A high- Q_{Lg} region is located in the northeastern Hangay Dome and corresponds to a series of basalts with ages from 6.0 to 12.8 Ma (Ancuta et al. 2018), possibly a solidified intrusive mafic magmatic body. Three longitudinal sections A–A' to C–C' and three latitudinal sections D–D' to F–F', with their locations shown in Fig. 7a, are selected to investigate the Hangay Dome and its surrounding areas. Profile A–A' is located along the western border of the Hangay Dome and shows two low- Q_{Lg} anomalies, with one in the western Gobi–Altai between 0.5 and 12 Hz and another in the Hovsgol rift between 0.5 and 3.0 Hz, and a third relatively low- Q_{Lg} anomalies along the Bulnay fault from 0.8 to 5.0 Hz. Profile B–B' crosses the interior of the Hangay Dome. It has two low- Q_{Lg} anomalies with one in the northeastern Hangay Dome from 0.5 to 12.0 Hz and another in the northeastern Hovsgol rift from 1.0 to 10.0 Hz, a third moderately low- Q_{Lg} anomaly along the South Hangay fault from 3.0 to 10.0 Hz, and a high- Q_{Lg} anomaly beneath the Gobi–Altai from 0.5 to 12.0 Hz. The high- Q_{Lg} anomaly corresponds to a high-resistivity region in the Gobi–Altai which has been considered as the residues left by the Valley of Lakes (Käufel et al. 2020). The easternmost profile C–C' has three low- Q_{Lg} anomalies, with the first beneath the south Hangay fault between 1.0 and 10.0 Hz, the second beneath the Togo volcano between 2.0 and 4.0 Hz and the third beneath the Hovsgol rift between 0.5 and 2.0 Hz, respectively. The interior of the Hangay Dome shows high- Q_{Lg} anomalies from 0.5 to 0.8 and 5.0 to 12.0 Hz. The latitudinal profile D–D' along the Bulnay fault also shows widespread low- Q_{Lg} anomalies from 0.5 to 5 Hz in the Mongolia–Altai, Valley of Lakes, and northern boundary of the Hangay Dome. The variations in Q_{Lg} values along the cross-section E–E' are less prominent, only showing relatively high- Q_{Lg} anomalies beneath the Hangay Dome. Profile F–F' shows high- Q_{Lg} anomalies in the Junggar Basin and several low- Q_{Lg} anomalies in the Mongolia–Altai and the South Hangay fault. Four major twentieth century earthquakes are located in regions with strong Q_{Lg} variations or low- Q_{Lg} values.

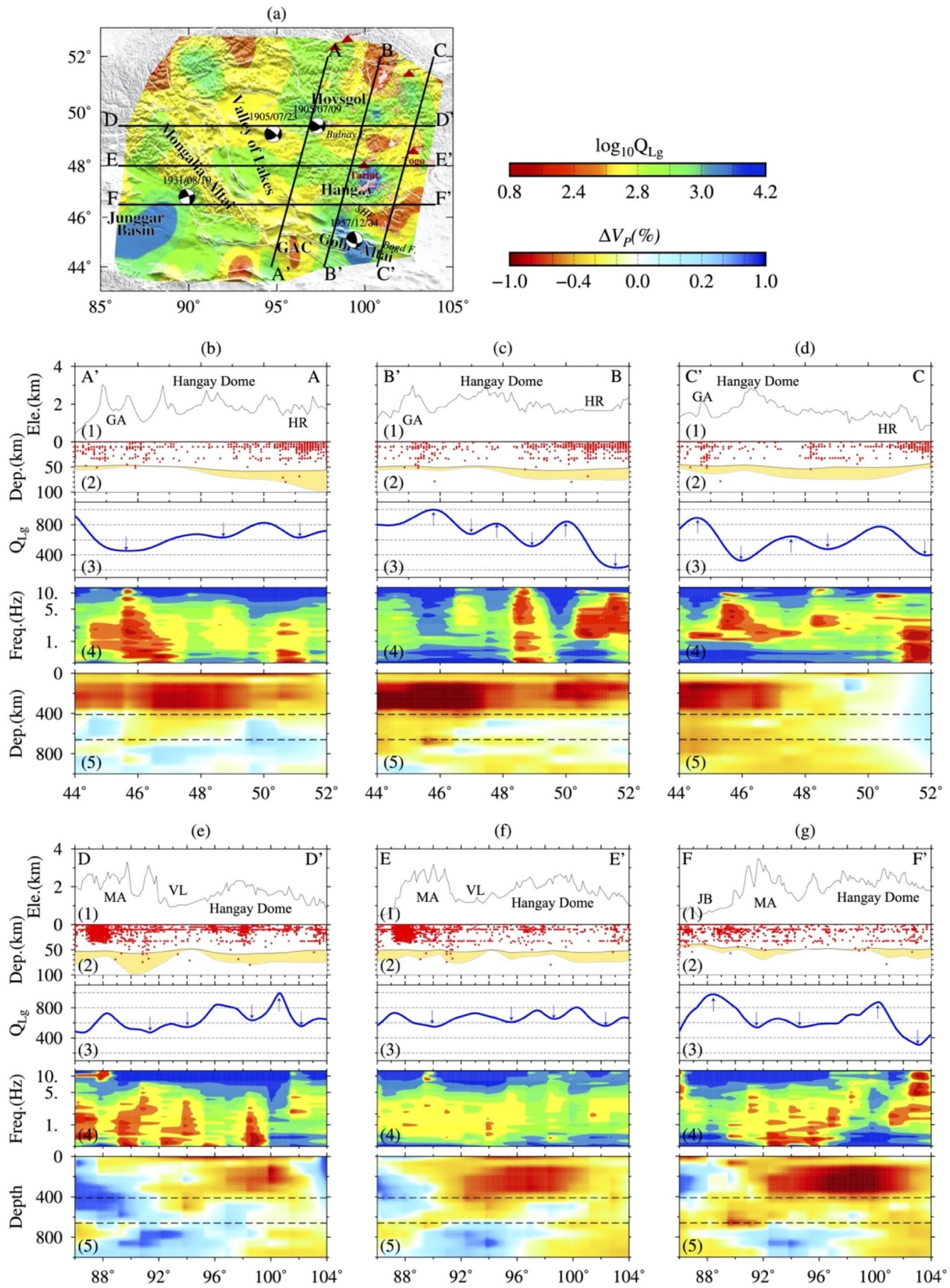


Fig. 7 **a** The broadband (1.5–6.0 Hz) Q_{Lg} map and locations of six cross sections. **b–g** Comparisons among various geological and geophysical properties along 6 profiles, including (1) surface topography, (2) crust and upper-mantle structures (the black line is the Moho discontinuity, the gray line is the LAB, and the yellow colored areas are the lithospheric mantle), and locations of earthquakes (red dots), (3) Q_{Lg} averaged between 1.5 and 6.0 Hz, (4) frequency-dependent Q_{Lg} between 0.5 and 12 Hz, and (5) percentage P-wave velocity perturbations from the MIT08 (Li et al. 2008) and the 410- and 660-km upper mantle discontinuities (dashed lines). The Moho discontinuity and the LAB are from the LITHO1.0 (Pasyanos et al. 2014). The earthquake locations are from the International Seismological Center (ISC)

Discussion

Thermal status of the crust constrained by strong Lg attenuation

The high-resolution broadband Q_{Lg} model in the Hangay Dome and its surroundings reveals remarkably strong heterogeneities in crustal attenuation. Overall, the interior of Hangay Dome and Gobi–Altai are characterized by high- Q_{Lg} values, whereas low- Q_{Lg} anomalies are also observed surrounding the Hangay Dome, especially in its eastern margin and the GAC. The Q_{Lg} variations result from the physical properties and thermal status of the crust, and are also affected by the geometrical parameters of crustal waveguide, such as changes in crustal thickness (Zhang and Lay 1995). The crustal thickness variation can partially explain the origin of low Q_{Lg} in the eastern margin of Hangay Dome, where crustal thinning exists (Feng 2021). However, such degree of crustal thinning may not be enough to explain the observed sharp decrease in Q_{Lg} from about 1000 to lower than 430. Furthermore, the observed low Q_{Lg} anomalies for eastern Hangay and the GAC coincide with anomalies of low-resistivity and low S-wave velocity in the crust (Käufel et al. 2020; Feng 2021), indicating that the Lg-wave dissipation in these two regions are probably dominated by the intrinsic attenuation associated with the thermal status and partial melting in the lower crust rather than just by scattering effects due to the intricate fault systems at the shallow depth and the crust thickness variations. The widespread relatively low- Q_{Lg} anomalies have been observed along the South Hangay fault and Bulnay fault. As the fault systems are usually the weakest zone in the crust and full of fractures of all scales, these low Q_{Lg} anomalies along the faults could be due to strong scattering. On the other hand, these low Q_{Lg} anomalies likely depict the channels that guide the partial melting materials move up vertically, similar to the phenomenon revealed by reflection seismology at the mid-ocean ridge where the partial melting materials generally move upward along the crustal faults (Singh et al. 2006). One way or another, the relatively low Q_{Lg} anomalies along the fault systems suggest that the margin of Hangay Dome is weak, which is also consistent with the local seismicity (Meltzer

et al. 2019). On the other hand, the high- Q_{Lg} anomalies in the center of the Hangay Dome are likely an indicator of the nucleus of the Precambrian block, which is still preserved although its eastern part has been modified by non-age-progressive, intermittent and sublithospheric mantle-sourced basaltic magmatism in the Cenozoic (Cunningham 2001; Ancuta et al. 2018).

Uplift mechanism of the Hangay Dome

The intracontinental uplift mechanism of the Hangay Dome has been discussed since the 1970s. Molnar and Tapponnier (1975) investigated the effects of the India–Eurasia collision and suggested that the far-field stress had deformed the Mongolia. However, based on the relief, lithospheric thickness, heat flow map, rift orientation, basaltic volcanism and thrusts of the Mongolia plateau, Windley and Allen (1993) suggested that the late Cenozoic uplift of the Mongolia was not externally driven by the India–Asia collision, but caused by the interaction of a mantle plume with overlying lithosphere. In the recent years, with the increasing observations, including seismic velocity tomography, geochemical investigations, magnetotelluric inversion, and S-wave receiver functions, more researchers preferred that the uplift of the Hangay Dome is driven by the asthenospheric upwelling and lithospheric removal (Barry et al. 2003; Chen et al. 2015; Käufel et al. 2020; Feng 2021; Zhao et al. 2021). The seismic velocity tomography showed a low-velocity zone in the upper mantle which could be the upwelling from the transition zone beneath the Hangay Dome (Chen et al. 2015). The magnetotelluric observations revealed that the low-resistivity regions extend from the asthenosphere to the lower crust of the Hangay Dome (Käufel et al. 2020). The petrogenesis of the Cenozoic basalts also suggested they were generated by small degrees of partial melting of an amphibole-bearing garnet peridotite source at depths > 70 km (Barry et al. 2003). All these studies tend to support asthenospheric upwellings in this region. The S-wave receiver functions indicated that the LAB is much shallower beneath the dome (~80–90 km) than in surrounding areas, such as the North China Craton (~150 km) and Siberian Craton (~180 km) (Zhao et al. 2021). The LITHO1.0 model also recorded lithospheric removals, and the lithospheric thinning areas corresponding to the low velocity anomalies in the upper mantle from MIT08 (Fig. 7). The low-velocity anomalies beneath the Hangay Dome should be reliable since the velocity anomalies are greater than the 5-degree resolution of the MIT08 in the upper mantle. Geodynamic modeling confirms the important role of lithospheric removal in the intraplate uplift of the Hangay Dome (Comeau et al. 2021). By comprehensively considering the attenuation result and those from other related studies, we prefer that the Hangay Dome uplift is caused by small-scale asthenospheric upwellings and lithospheric removals. The strong crustal attenuation in the eastern margin of

the Hangay Dome and GAC may indicate the location where the small-scale mantle material intrusion happens. The crust thermal status also suggests that the upwelling asthenospheric materials further deform the Hangay Dome and its surroundings, and lead to widespread Cenozoic volcanism and active seismicity in this region.

Conclusion

A broadband high-resolution Lg-wave attenuation model was developed for the Hangay Dome and its surrounding regions based on the data from XL seismic array deployed by the Central Mongolia Seismic Experiment and other permanent stations of the IRIS and CENC. Comparing to previous studies in this region, the new Q_{Lg} model extended the frequency range to 0.1–20.0 Hz and increased the best resolution to $\sim 1.0^\circ \times 1.0^\circ$ between 0.4 and 6.0 Hz. This Q model provided a better constraint to underlying processes with a much broader frequency band and finer scale. The revealed Lg-wave attenuation variations correlated well with regional tectonic activities. Several strong Lg attenuation anomalies were observed around the Hangay Dome, especially in its eastern part where Cenozoic basalts were widely exposed at the surface. The distributions of low Q_{Lg} values around the Hangay Dome possibly imply that the margin of the Hangay Dome has been deformed. High Q_{Lg} values observed at the center of the Hangay Dome suggested that the interior of the Hangay Dome is the residual nucleus.

Supplementary Information The online version contains supplementary material available at <https://doi.org/10.1007/s00531-021-02131-8>.

Acknowledgements The comments from the Chief Editor Wolf-Christian Dulló and two anonymous reviewers are valuable and greatly improved this manuscript. The broadband data used in this study were retrieved from the China Earthquake Network Center (CENC) and the Incorporated Research Institutions for Seismology Data Management Center (IRIS DMC). Some figures were created using the generic mapping tools (GMTs) (Wessel et al. 2019). This research was supported by the National Key Research and Development Program of China (2017YFC0601206) and the National Natural Science Foundation of China (41974061, 41974054, 41630210, and 41674060).

References

- Ancuta LD, Zeitler PK, Idleman BD, Jordan BT (2018) Whole-rock $^{40}\text{Ar}/^{39}\text{Ar}$ geochronology, geochemistry, and stratigraphy of intraplate Cenozoic volcanic rocks, central Mongolia. *GSA Bull* 128:1397–1408. <https://doi.org/10.1130/B31788.1>
- Bao X, Sandvol E, Chen YJ, Ni J, Hearn T, Shen Y (2012) Azimuthal anisotropy of Lg attenuation in eastern Tibetan Plateau. *J Geophys Res Solid Earth* 117:1–14. <https://doi.org/10.1029/2012JB009255>
- Barry TL, Saunders AD, Kempton PD, Windley BF, Pringle MS, Dor-namjaa D, Saandar S (2003) Petrogenesis of Cenozoic basalts from Mongolia: evidence for the role of asthenospheric versus metasomatized lithospheric mantle sources. *J Petrol* 44:55–91. <https://doi.org/10.1093/ptrology/44.1.55>
- Bayasgalan A, Jackson J, Ritz JF, Carretier S (1999) Field examples of strike–slip fault terminations in Mongolia and their tectonic significance. *Tectonics* 18:394–411. <https://doi.org/10.1029/1999TC900007>
- Benz HM, Frankel A, Boore DM (1997) Regional Lg attenuation for the continental United States. *B Seismol Soc Am* 87:606–619. <http://pubs.er.usgs.gov/publication/70019752>.
- Brune JN (1970) Tectonic stress and the spectra of seismic shear waves from earthquakes. *J Geophys Res* 75:4997–5009. <https://doi.org/10.1029/JB075i026p04997>
- Calais E, Vergnolle M, San'kov V, Lukhnev A, Miroshnitchenko A, Amarjargal S, Déverchère J (2003) GPS measurements of crustal deformation in the Baikal–Mongolia area (1994–2002): implications for current kinematics of Asia. *J Geophys Res Solid Earth* 108:1481–1503. <https://doi.org/10.1029/2002JB002373>
- Castro RR, Anderson JG, Singh SK (1990) Site response, attenuation and source spectra of S waves along the Guerrero, Mexico, subduction zone. *B Seismol Soc Am* 80:1481–1503. <https://doi.org/10.1785/BSSA08006A1481>
- Chen M, Niu F, Liu Q, Tromp J (2015) Mantle-driven uplift of Hangay Dome: new seismic constraints from adjoint tomography. *Geophys Res Lett* 42:6967–6974. <https://doi.org/10.1002/2015GL065018>
- Comeau MJ, Stein C, Becken M, Hansen U (2021) Geodynamic modeling of lithospheric removal and surface deformation: application to intraplate uplift in Central Mongolia. *J Geophys Res Solid Earth* 126:e2020JB021304. <https://doi.org/10.1029/2020JB021304>
- Cunningham WD (2001) Cenozoic normal faulting and regional doming in the southern Hangay region, Central Mongolia: Implications for the origin of the Baikal rift province. *Tectonophysics* 331:389–411. [https://doi.org/10.1016/S0040-1951\(00\)00228-6](https://doi.org/10.1016/S0040-1951(00)00228-6)
- Feng L (2021) High-resolution crustal and uppermost mantle structure beneath central Mongolia from rayleigh waves and receiver functions. *J Geophys Res Solid Earth* 126:1–18. <https://doi.org/10.1029/2020JB021161>
- Fuch S, Norden B, Commission IHF (2021) The global heat flow database: release 2021. GFZ Data Serv. <https://doi.org/10.5880/idgeo.2021.014>
- Furumura T, Kennett BLN (1997) On the nature of regional seismic phases—II. On the influence of structural barriers. *Geophys J Int* 129:221–234. <https://doi.org/10.1111/j.1365-246X.1997.tb01577.x>
- Gallegos A, Ranasinghe N, Ni J, Sandvol E (2014) Lg attenuation in the central and eastern United States as revealed by the EarthScope Transportable Array. *Earth Planet Sc Lett* 402:187–196. <https://doi.org/10.1016/j.epsl.2014.01.049>
- Goldstein P, Snoko A (2005) SAC availability for the IRIS community. Incorporated Institutions for Seismology Data Management Center Electronic Newsletter 7
- Guang-Yin X, Su-Yun W, Wen-Lin H, Lin W, Jia GA, Demberel S (2014) Study on seismicity and its geodynamic genesis in Sino-Mongolia Arc Areas. *Chin J Geophys* 57:2372–2385. <https://doi.org/10.6038/cjg20140731>
- He J, Sandvol E, Wu Q, Gao M, Gallegos A, Ulziibat M, Demberel S (2017) Attenuation of regional seismic phases (Lg and Sn) in Eastern Mongolia. *Geophys J Int* 211:979–989. <https://doi.org/10.1093/gji/ggx349>
- He X, Zhao LF, Xie XB, Tian X, Yao ZX (2021) Weak crust in south-east Tibetan Plateau revealed by Lg-wave attenuation tomography: implications for crustal material escape. *J Geophys Res Solid Earth* 126:1–17. <https://doi.org/10.1029/2020JB020748>

- Herrmann RB, Kijko A (1983) Short-period Lg magnitudes: Instrument, attenuation, and source effects. *B Seismol Soc Am* 73:1835–1850. <https://doi.org/10.1785/BSSA07306A1835>
- Käuffl JS, Grayver AV, Comeau MJ, Kuvshinov AV, Becken M, Kamm J, Batmagnai E, Demberel S (2020) Magnetotelluric multiscale 3-D inversion reveals crustal and upper mantle structure beneath the Hangai and Gobi–Altai region in Mongolia. *Geophys J Int* 221:1002–1028. <https://doi.org/10.1093/gji/ggaa039>
- Kaviani A, Sandvol E, Bao X, Rümpker G, Gök R (2015) The structure of the crust in the Turkish–Iranian Plateau and Zagros using Lg Q and velocity. *Geophys J Int* 200:1254–1268. <https://doi.org/10.1093/gji/ggu468>
- Knopoff L, Schwab F, Kauselt E (1973) Interpretation of Lg*. *Geophys J Int* 33:389–404. <https://doi.org/10.1111/j.1365-246X.1973.tb02375.x>
- Laske G, Masters G, Ma Z, Pasyanos M (2013) Update on CRUST1.0 – A 1-degree Global Model of Earth's Crust. *Geophys Res Abstracts* 15, Abstract EGU2013-2658
- Li C, van der Hilst RD, Engdahl ER, Burdick S (2008) A new global model for P wave speed variations in Earth's mantle. *Geochem Geophys Geosyst* 9:Q05018. <https://doi.org/10.1029/2007GC001806>
- Liu X, Zhao D, Li S (2014) Seismic attenuation tomography of the Northeast Japan arc: Insight into the 2011 Tohoku earthquake (Mw 9.0) and subduction dynamics. *J Geophys Res Solid Earth* 119:1094–1118. <https://doi.org/10.1002/2013JB010591>
- Luo Y, Zhao L-F, Ge Z-X, Xie X-B, Yao Z-X (2021) Crustal Lg-wave attenuation in Southeast Asia and its implications for regional tectonic evolution. *Geophys J Int* 226:1873–1884. <https://doi.org/10.1093/gji/ggab122>
- Meltzer A, Stachnik JC, Sodnomsambuu D, Munkhuu U, Tsagaan B, Dashdondog M, Russo R (2019) The central Mongolia seismic experiment: multiple applications of temporary broadband seismic arrays. *Seismol Res Lett* 90:1364–1376. <https://doi.org/10.1785/0220180360>
- Mitchell BJ (1995) Anelastic structure and evolution of the continental crust and upper mantle from seismic surface wave attenuation. *Rev Geophys* 33:441–462. <https://doi.org/10.1029/95RG02074>
- Mitchell BJ, Hwang HJ (1987) Effect of low Q sediments and crustal Q on Lg attenuation in the United States. *B Seismol Soc Am* 77:1197–1210. <https://doi.org/10.1785/BSSA0770041197>
- Mitchell BJ, Pan Y, Xie J, Cong L (1997) Lg coda Q variation across Eurasia and its relation to crustal evolution. *J Geophys Res Solid Earth* 102:22767–22779. <https://doi.org/10.1029/97JB01894>
- Mitchell BJ, Cong L, Ekström G (2008) A continent-wide map of 1-Hz Lg coda Q variation across Eurasia and its relation to lithospheric evolution. *J Geophys Res Solid Earth* 113:1–19. <https://doi.org/10.1029/2007JB005065>
- Molnar P, Tapponnier P (1975) Cenozoic tectonics of Asia: effects of a continental collision. *Science* 189:419–426. <https://doi.org/10.1126/science.189.4201.419>
- Morgan JV, Christeson GL, Zelt CA (2002) Testing the resolution of a 3D velocity tomogram across the Chicxulub crater. *Tectonophysics* 355:215–226. <https://www.sciencedirect.com/science/article/pii/S0040195102001439>
- Ottmöller L (2002) Lg wave Q tomography in Central America. *Geophys J Int* 150:295–302. <https://ui.adsabs.harvard.edu/abs/2002GeoJI.150..295O>
- Ottmöller L, Shapiro NM, Krishna Singh S, Pacheco JF (2002) Lateral variation of Lg wave propagation in southern Mexico. *J Geophys Res Sol Earth*. <https://doi.org/10.1029/2001JB000206>
- Paige CC, Saunders MA (1982) LSQR: an algorithm for sparse linear equations and sparse least squares. *ACM Trans Math Softw* 8:43–71. <https://doi.org/10.1145/355984.355989>
- Pasyanos ME, Matzel EM, Walter WR, Rodgers AJ (2009) Broadband Lg attenuation modelling in the Middle East. *Geophys J Int* 177:1166–1176. <https://doi.org/10.1111/j.1365-246X.2009.04128.x>
- Pasyanos ME, Masters TG, Laske G, Ma ZT (2014) LITHO1.0: an updated crust and lithospheric model of the Earth. *J Geophys Res Solid Earth* 119:2153–2173. <https://doi.org/10.1002/2013JB010626>
- Phillips WS, Hartse HE, Rutledge JT (2005) Amplitude ratio tomography for regional phase Q. *Geophys Res Lett* 32:1–4. <https://doi.org/10.1029/2005GL023870>
- Rapine RR, Ni JF (2003) Propagation characteristics of Sn and Lg in northeastern China and Mongolia. *B Seismol Soc Am* 93:939–945. <https://doi.org/10.1785/0120010157>
- Ringdal F, Marshall PD, Alewine RW (1992) Seismic yield determination of Soviet underground nuclear explosions at the Shagan River test site. *Geophys J Int* 109:65–77. <https://doi.org/10.1111/j.1365-246X.1992.tb00079.x>
- Rizza M, Ritz JF, Braucher R, Vassallo R, Prentice C, Mahan S, McGill S, Chauvet A, Marco S, Todbileg M, Demberel S, Bourlès D (2011) Slip rate and slip magnitudes of past earthquakes along the Bogd left-lateral strike–slip fault (Mongolia). *Geophys J Int* 186:897–927. <https://doi.org/10.1111/j.1365-246X.2011.05075.x>
- Rizza M, Ritz JF, Prentice C, Vassallo R, Braucher R, Larroque C, Arzhannikova A, Arzhannikov S, Mahan S, Massault M, Michelot JL, Todbileg M, Arnold M, Aumaître G, Bourlès D, Keddadouche K (2015) Earthquake geology of the Bulnay fault (Mongolia). *B Seismol Soc Am* 105:72–93. <https://doi.org/10.1785/0120140119>
- Schlittenhardt J (2001) Teleseismic Lg of semipalatinsk and novaya zemlya nuclear explosions recorded by the GRF (Gräfenberg) array: comparison with regional Lg (BRV) and their potential for accurate yield estimation. *Pure Appl Geophys* 158:2253–2274. <https://doi.org/10.1007/PL00001148>
- Sengor AMC, Natalin BA, Burtman VS (1993) Evolution of the altaid tectonic collage and Paleozoic crustal growth in Eurasia. *Nature* 364:299–307. <https://doi.org/10.1038/364299a0>
- Singh SC, Crawford WC, Carton H, Seher T, Combier V, Cannat M, Pablo Canales J, Düsünür D, Escartin J, Miguel Miranda J (2006) Discovery of a magma chamber and faults beneath a Mid-Atlantic Ridge hydrothermal field. *Nature* 442:1029–1032. <https://doi.org/10.1038/nature05105>
- Street RL, Herrmann RB, Nuttli OW (1975) Spectral Characteristics of the Lg wave Generated by Central United States Earthquakes. *Geophys J Int* 41:51–63. <https://doi.org/10.1111/j.1365-246X.1975.tb05484.x>
- Taylor SR, Yang X, Phillips WS (2003) Bayesian Lg attenuation tomography applied to Eastern Asia. *B Seismol Soc Am* 93:795–803. <https://doi.org/10.1785/0120020010>
- Wessel P, Luis JF, Uieda L, Scharroo R, Wobbe F, Smith WHF, Tian D (2019) The generic mapping tools version 6. *Geochem Geophys Geosyst* 20:5556–5564. <https://doi.org/10.1029/2019GC008515>
- Windley BF, Allen MB (1993) Mongolian Plateau: evidence for a late Cenozoic mantle plume under central Asia. *Geology* 21:295–298. [https://doi.org/10.1130/0091-7613\(1993\)021%3c0295:MPEFAL%3e2.3.CO;2](https://doi.org/10.1130/0091-7613(1993)021%3c0295:MPEFAL%3e2.3.CO;2)
- Windley BF, Alexeiev D, Xiao WJ, Kroner A, Badarch G (2007) Tectonic models for accretion of the Central Asian Orogenic Belt. *J Geol Soc* 164:31–47. <https://doi.org/10.1144/0016-76492006-022>
- Xiao WJ, Windley BF, Han CM, Liu W, Wan B, Zhang J, Ao SJ, Zhang ZY, Song DF (2018) Late Paleozoic to early Triassic multiple roll-back and oroclinal bending of the Mongolia

- collage in Central Asia. *Earth-Sci Rev* 186:94–128. <https://doi.org/10.1016/j.earscirev.2017.09.020>
- Xie X-B, Lay T (1994) The excitation of Lg waves by explosions: a finite-difference investigation. *B Seismol Soc Am* 84:324–342
- Xie J, Gok R, Ni J, Aoki Y (2004) Lateral variations of crustal seismic attenuation along the INDEPTH profiles in Tibet from Lg Q inversion. *J Geophys Res Solid Earth* 109:1–17. <https://doi.org/10.1029/2004JB002988>
- Xie J, Wu Z, Liu R, Schaff D, Liu Y, Liang J (2006) Tomographic regionalization of crustal Lg Q in eastern Eurasia. *Geophys Res Lett* 33:2–5. <https://doi.org/10.1029/2005GL024410>
- Zelt CA (1998) Lateral velocity resolution from three-dimensional seismic refraction data. *Geophys J Int* 135:1101–1112. <https://doi.org/10.1046/j.1365-246X.1998.00695.x>
- Zhang T-R, Lay T (1995) Why the Lg phase does not traverse oceanic crust. *B Seismol Soc Am* 85:1665–1678
- Zhao LF, Mousavi SM (2018) Lateral variation of crustal Lg attenuation in Eastern North America. *Sci Rep UK* 8:7285. <https://doi.org/10.1038/s41598-018-25649-5>
- Zhao LF, Xie XB (2016) Strong Lg-wave attenuation in the Middle East continental collision orogenic belt. *Tectonophysics* 674:135–146. <https://doi.org/10.1016/j.tecto.2016.02.025>
- Zhao LF, Xie XB, Wang WM, Yao ZX (2008) Regional seismic characteristics of the 9 October 2006 North Korean nuclear test. *B Seismol Soc Am* 98:2571–2589. <https://doi.org/10.1785/0120080128>
- Zhao LF, Xie XB, Wang WM, Zhang JH, Yao ZX (2010) Seismic Lg-wave Q tomography in and around Northeast China. *J Geophys Res Solid Earth* 115:B08307. <https://doi.org/10.1029/2009JB007157>
- Zhao LF, Xie XB, He JK, Tian XB, Yao ZX (2013a) Crustal flow pattern beneath the Tibetan Plateau constrained by regional Lg-wave Q tomography. *Earth Planet Sc Lett* 383:113–122. <https://doi.org/10.1016/j.epsl.2013.09.038>
- Zhao LF, Xie XB, Wang WM, Zhang JH, Yao ZX (2013b) Crustal Lg attenuation within the North China Craton and its surrounding regions. *Geophys J Int* 195:513–531. <https://doi.org/10.1093/gji/ggt235>
- Zhao H, Wang P, Huang Z (2021) Lithospheric structures beneath the western Mongolian Plateau: Insight from S wave receiver function. *J Asian Earth Sci* 212:104733–104733. <https://doi.org/10.1016/j.jseaes.2021.104733>
- Zhou L, Zhao C, Chen Z, Zheng S (2011) Amplitude tomography of Lg waves in Xinjiang and Its adjacent regions. *B Seismol Soc Am* 101:1302–1314. <https://doi.org/10.1785/0120100267>
- Zor E, Sandvol E, Xie J, Türkelli N, Mitchell B, Gasanov AH, Yetirmishli G (2007) Crustal attenuation within the Turkish Plateau and surroundings regions. *B Seismol Soc Am* 97:151–161. <https://doi.org/10.1785/0120050227>